

# Efficient Light-Driven Ion Pumping for Deep Desalination via the Vertical Gradient Protonation of Covalent Organic Framework Membranes

Weipeng Xian, Xiaoyi Xu, Yongxin Ge, Zhiwei Xing, Zhuozhi Lai, Qing-Wei Meng, Zhifeng Dai, Sai Wang,\* Ruotian Chen, Ning Huang, Shengqian Ma, and Qi Sun\*



Cite This: *J. Am. Chem. Soc.* 2024, 146, 33973–33982



Read Online

ACCESS |



Metrics & More

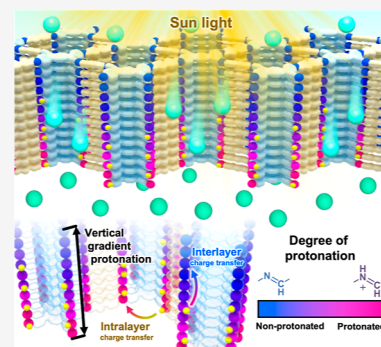


Article Recommendations



Supporting Information

**ABSTRACT:** Traditional desalination methods face criticism due to high energy requirements and inadequate trace ion removal, whereas natural light-driven ion pumps offer superior efficiency. Current synthetic systems are constrained by short exciton lifetimes, which limit their ability to generate sufficient electric fields for effective ion pumping. We introduce an innovative approach utilizing covalent-organic framework membranes that enhance light absorption and reduce charge recombination through vertical gradient protonation of imine linkages during acid-catalyzed liquid–liquid interfacial polymerization. This technique creates intralayer and interlayer heterojunctions, facilitating interlayer hybridization and establishing a robust built-in electric field under illumination. These improvements enable the membranes to achieve remarkable ion transport across extreme concentration gradients (2000:1), with a transport rate of approximately  $3.2 \times 10^{12}$  ions per second per square centimeter and reduce ion concentrations to parts per billion. This performance significantly surpasses that of conventional reverse osmosis systems, representing a major advancement in solar-powered desalination technology by substantially reducing energy consumption and secondary waste.



## INTRODUCTION

Deionized water is essential across various sectors, including electronic manufacturing, pharmaceuticals, and boiler water supply, where it impacts both product quality and operational efficiency.<sup>1–4</sup> The predominant method for deionizing water is reverse osmosis, a process known for its extensive energy consumption and limited ability to reduce ion concentrations to only a few parts per million (ppm).<sup>5,6</sup> When even lower ion levels are required, industries typically turn to ion-exchange resins. Although effective at removing ions, these resins produce substantial secondary waste and necessitate frequent, labor-intensive chemical regeneration.<sup>7</sup> Alternative methods like electrochemical deionization reduce reliance on chemicals but still suffer from low ion removal rates and high energy usage.<sup>8,9</sup> These limitations highlight the critical need for more efficient and environmentally friendly solutions, especially for the last-mile desalination of water with exceptionally low salt concentrations. In nature, biological ion pumps that move ions against concentration gradients using light energy provide an intriguing blueprint for innovation.<sup>10,11</sup> By emulating these natural processes, significant advancements in water desalination can be achieved. Although various synthetic membrane systems designed as ion pumps have been explored for energy conversion and storage, their application in desalination is limited.<sup>12–25</sup> This is largely due to their insufficient ability to handle large concentration gradients—often only up to a 50-

fold difference—compounded by poor light absorption and brief exciton lifetimes, as well as light-induced transmembrane potential, which is thought to be at the heart of the pumping phenomenon (Table S1).

Covalent organic frameworks (COFs) are crystalline, porous materials distinguished by their versatility in membrane applications.<sup>26–37</sup> Their customizable properties enable precise control over charge transfer behaviors by integrating functional building blocks into a covalently bonded periodic structure. These materials find extensive use in light-responsive applications like photocatalysis and photothermal processes.<sup>38–48</sup> Current research focuses on enhancing intralayer charge transfer by employing topology-guided conjugation and incorporating donor and acceptor units within their lattice structures.<sup>49–51</sup> This approach tends to confine electrons and holes within individual layers, causing significant overlap and reducing the lifetimes of these charge carriers. To address this issue, the concept of interlayer-hybridized excitons has been

**Received:** September 16, 2024

**Revised:** November 20, 2024

**Accepted:** November 21, 2024

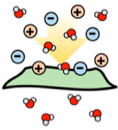
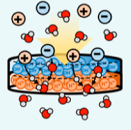
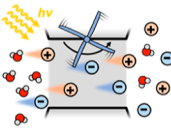
**Published:** November 28, 2024



introduced, designed to prolong their lifespan and increase their population by capitalizing on the robust light interaction properties of intralayer excitons combined with the longer lifetimes of spatially indirect interlayer excitons.<sup>52,53</sup> Although 2D COFs naturally tend toward electronic hybridization across layers due to their delocalized orbitals in the out-of-plane direction, fine-tuning these layer-hybridized excitons to enhance interlayer hybridization remains a significant challenge due to the intricate integration required between two distinct membrane materials with unique band structures and interfacial properties.

Building on recent advancements that demonstrate how protonating imine linkages within COFs can significantly boost light conversion efficiency by enhancing light absorption and extending exciton lifetimes, we propose creating a vertical protonation gradient within COF membranes.<sup>54–57</sup> This strategy could promote interlayer hybridization through the formation of both intralayer and interlayer heterojunction structures, exploiting the energy band differences between imine-linked building blocks and their protonated counterparts. Furthermore, the lattice-matched eclipsed  $\pi$ - $\pi$  stacking of the 2D COF layers minimizes energy losses, optimizing the process. Indeed, COF membranes with a vertical protonation gradient not only improve light absorption but also enhance electron–hole separation. This results in a greatly enhanced light-induced electric field, which substantially increases the efficiency of ion pumping. Our innovative approach of implementing a vertical gradient protonation in COF-based membranes allows them to transport various salts against concentration gradients by as much as 2000 times. This offers a promising, sustainable, and energy-efficient solution for applications like desalination (Table 1).

**Table 1. Summary of Features for Three Desalination Methods: Reverse Osmosis, Ion Exchange, and Light-Driven Ion Pump**

Desalination method			
Driving Force	Pressure	Concentration gradient	Light
Ion removal efficiency	Moderate	High	High
Environment impact	Low	High	Low
Energy requirement	High	Low	Low <sup>(a)</sup>

<sup>a</sup>The light source can be sunlight. The energy requirement refers specifically to the energy consumption during the desalination process.

## RESULTS AND DISCUSSION

**Synthesis and Structural Analysis.** To evaluate the feasibility of our approach and investigate the role of imine linkage protonation, we conducted a proof-of-concept study using 1,3,6,8-tetrakis(4-aminophenyl)pyrene (Py) and various thiophene dicarbaldehydes. These components were selected for their minimal donor–acceptor contrast and enhanced electron density at the imine sites, facilitating protonation. Pyrene was chosen for its robust light-absorbing capabilities.

Given that acid-catalyzed condensation between carbonyl compounds and primary amines initially produces protonated imine bonds, which then undergo deprotonation,<sup>58</sup> we hypothesized that controlling membrane distribution across acidic aqueous and organic phases could establish a protonation gradient. Contact with the acidic solution inhibits deprotonation, while removal of the acid allows deprotonation to proceed. To achieve this, we employed acid-catalyzed liquid–liquid interfacial polymerization (Figure 1a). As the membrane formed at the water–oil interface and expanded outward, the degree of deprotonation increased with the distance from the acidic solution, creating a protonation gradient. To investigate this mechanism, we dissolved Py in various concentrations of aqueous acetic acid, while 2,2'-bithiophenyl-5,5'-dicarbaldehyde (Ta) was dissolved in a mixture of mesitylene and ethyl acetate. These biphasic solutions were incubated at 35 °C for 3 days in sealed vials, resulting in optically uniform, glossy membranes. The intensity of membrane coloration deepened with increasing acetic acid concentration (Figure S1). Scanning electron microscopy (SEM) revealed a dense, void-free surface morphology, with membrane thickness ranging from 150 to 800 nm (Figures 1b and S2–S5), dependent on the acid and monomer concentrations used. Detailed information about the membrane prepared using 3 M acetic acid is provided in the main text (referred to as COF-PyTa), with other variants detailed in the Supporting Information.

Nanoindentation tests conducted on the COF-PyTa membrane demonstrated a hardness value of 18.2 MPa, indicating a commendable level of mechanical strength (Figure S6). Transmission electron microscopy (TEM) indicated locally ordered one-dimensional pore channels with a pore size of 1.7 nm, characteristic of a porous crystalline structure (Figure S7). N<sub>2</sub> sorption analysis confirmed the microporous nature of the COF-PyTa membrane, which exhibited a Brunauer–Emmett–Teller (BET) surface area of 468 m<sup>2</sup> g<sup>-1</sup> (Figure S8). Attenuated total reflectance Fourier transform infrared spectroscopy (ATR-FTIR) characterized the COF-PyTa membrane, highlighting a prominent IR band at approximately 1612 cm<sup>-1</sup> attributed to the stretching vibration of the –C=N– bond.<sup>59</sup> This observation, combined with the significant reduction in NH<sub>2</sub> group vibrations at 3300–3400 cm<sup>-1</sup> in the Py spectrum and the aldehyde stretching vibration of Ta at 1650 cm<sup>-1</sup>, indicated extensive Schiff base condensation (Figure S9). Comparative ATR-FTIR analysis of the COF-PyTa membrane segments facing the organic phase (COF-PyTa(O)) versus the acid aqueous phase (COF-PyTa(W)) revealed distinct differences, particularly at 1735, 1665, and 1612 cm<sup>-1</sup>. COF-PyTa(O) exhibited a stronger peak at 1612 cm<sup>-1</sup>, while COF-PyTa(W) demonstrated enhanced intensities at 1735 and 1665 cm<sup>-1</sup>, corresponding to the protonated –C=NH<sup>+</sup>– and –C=O– stretch from acetate ions, respectively (Figure 1c).<sup>60</sup> This demonstrated varying degrees of imine linkage protonation by acetic acid across different sections of the membrane. Water contact angle tests further indicated increased hydrophilicity on the protonated side of the membrane compared to the non-protonated side (Figure S10).

To further explore the asymmetric protonation gradient across the COF-PyTa membrane, X-ray photoelectron spectroscopy (XPS) was utilized to analyze the chemical states of nitrogen species on both the COF-PyTa(O) and COF-PyTa(W) sides. XPS, known for its depth sensitivity to

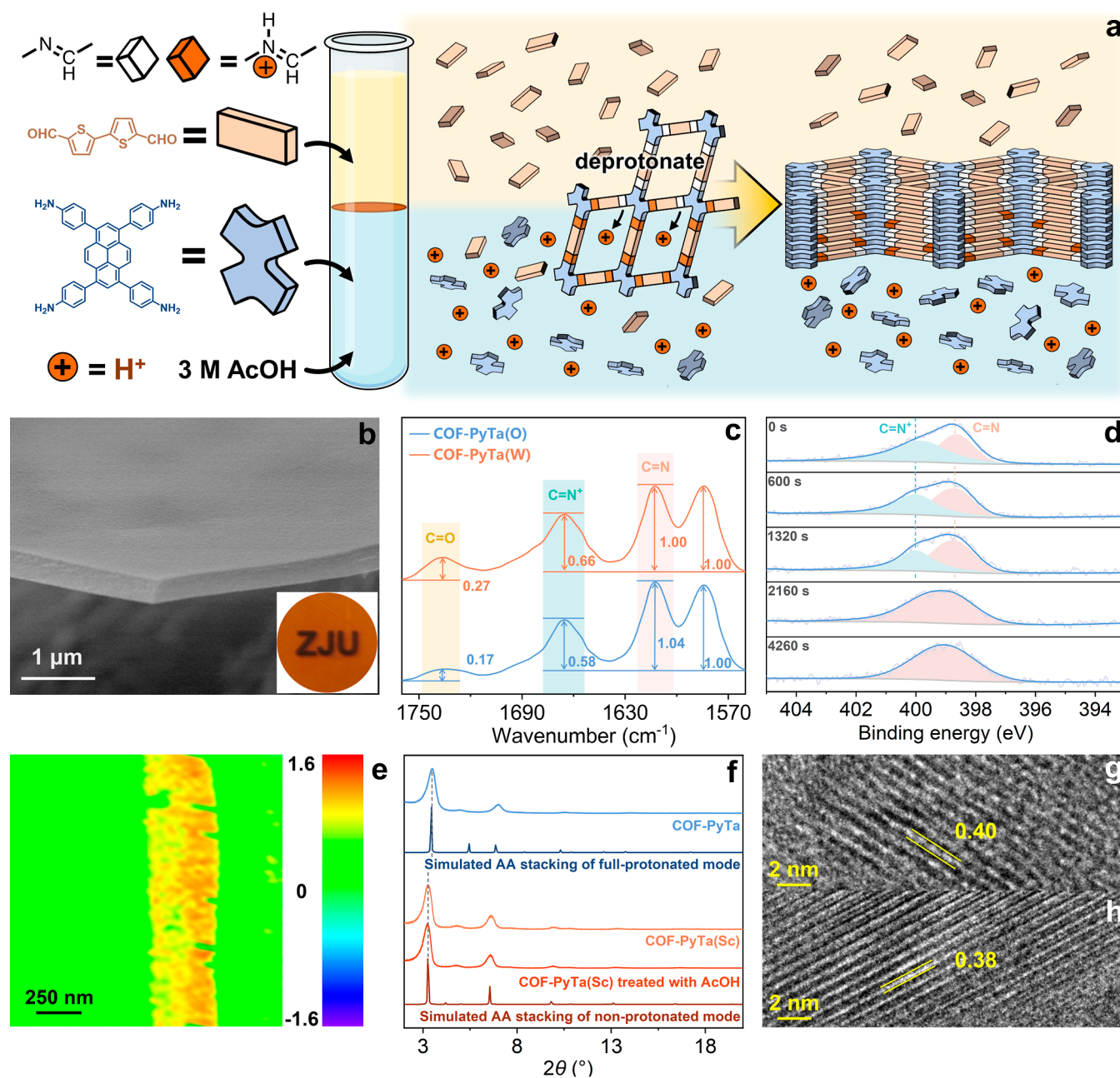


**Figure 1.** Membrane synthesis and characterization. (a) Schematic representation of acid-catalyzed liquid–liquid interfacial polymerization used for creating a vertical gradient (perpendicular to the membrane plane) of protonation in the imine linkages across the membrane. (b) SEM image of the COF-PyTa membrane; inset shows a photograph of the membrane. (c) ATR-FTIR spectra comparing COF-PyTa(O) and COF-PyTa(W). (d) XPS spectra of the COF-PyTa membrane following sequential etching with Ar<sup>+</sup> ions at various durations from the COF-PyTa(W) to the COF-PyTa(O) side. (e) AFM-IR intensity maps at 1665 cm<sup>-1</sup> showing the distribution across the membrane cross-section. (f) PXRD patterns illustrating crystalline structure variations. (g,h) TEM images of COF-PyTa and COF-PyTa(Sc), respectively.

elemental composition and chemical states up to about 3–5 nm from the surface, helped in distinguishing the sides. The N 1s XPS spectra showed clear differences: a single peak at 399.2 eV was observed on the COF-PyTa(O) side, indicative of the  $-\text{C}=\text{N}-$  configuration, while the COF-PyTa(W) side displayed peaks at 398.7 eV ( $-\text{C}=\text{N}-$ ) and 399.8 eV (protonated  $-\text{C}=\text{NH}^+-$ ) (Figures 1d and S11).<sup>61</sup> To visualize the distribution of the protonated amine  $-\text{C}=\text{NH}^+-$  within the membrane, atomic force microscope-infrared spectroscopy (AFM-IR) intensity maps were produced at 1665 cm<sup>-1</sup> across the membrane cross-section. This analysis identified distinct layers with more pronounced AFM-IR

signals on the COF-PyTa(W) side, penetrating about halfway through the membrane (Figure 1e). To verify that the 1665 cm<sup>-1</sup> peak on the COF-PyTa(O) side was not attributable to protonated amine groups, we synthesized the COF-PyTa powder under solvothermal conditions without added acid, which minimized acid-related effects. This powder also exhibited a 1665 cm<sup>-1</sup> IR band, albeit with a lower intensity. We attribute the higher intensity observed on the COF-PyTa(O) side to the greater penetration capabilities of ATR-FTIR, which can detect protonated layers more effectively within the membrane (Figure S12). For a quantitative assessment of the protonation gradient, Ar<sup>+</sup> ion etching was

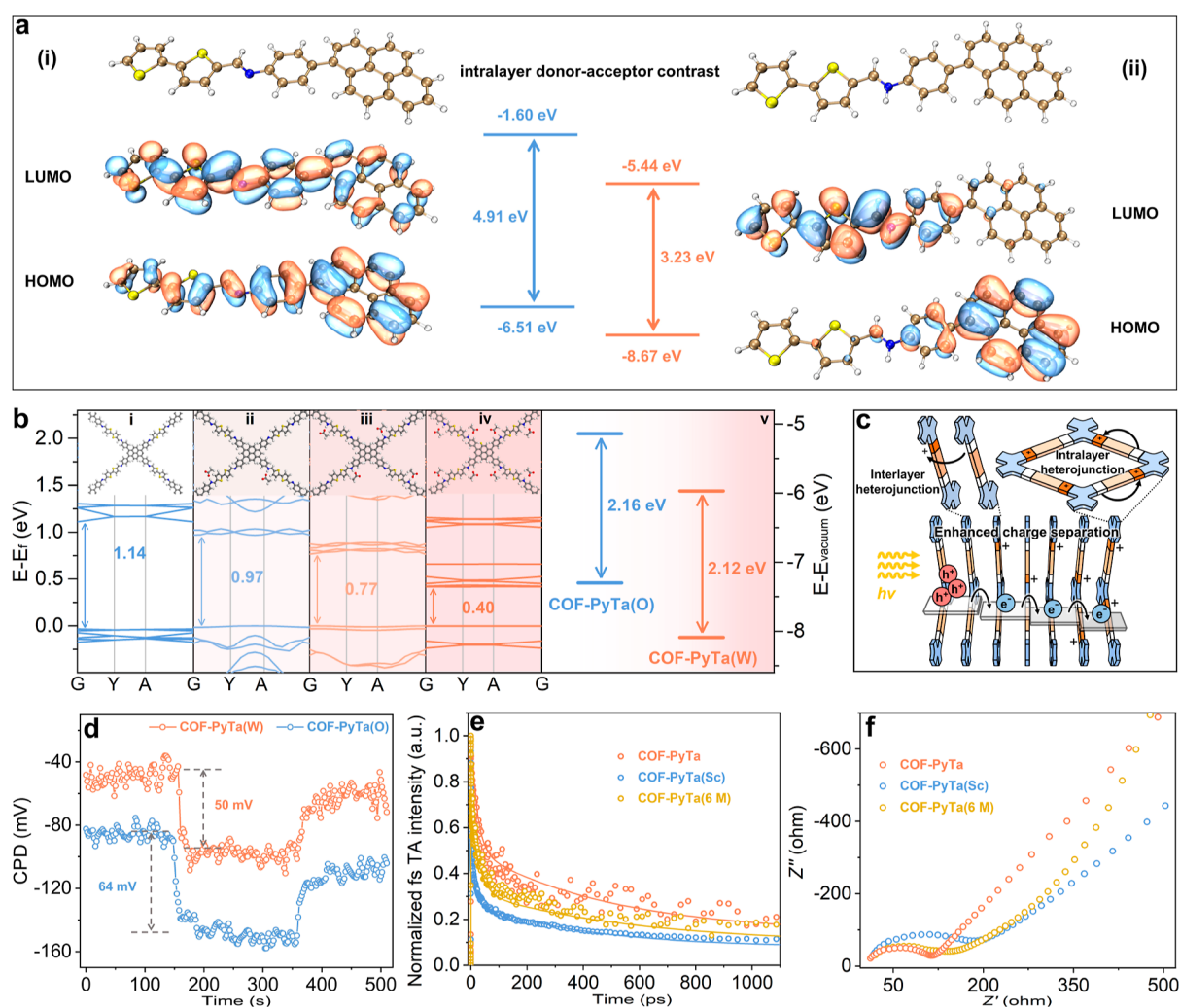


**Figure 2.** Analysis of optical properties. (a) NTO particle–hole diagrams for (i) nonprotonated and (ii) protonated segments of COF-PyTa, illustrating electron distribution variations (gold; C, blue; N, yellow; S, and white; H). (b) Band structure evolution with varying protonation levels of imine linkages: (i) nonprotonated, (ii) 1/4 protonated, (iii) 1/2 protonated, and (iv) fully protonated, including (v) energy level alignments showing differences between COF-PyTa(W) and COF-PyTa(O). (c) Schematic representation of intralayer and interlayer heterojunction structures enhancing charge separation. (d) CPD measurements for COF-PyTa(W) and COF-PyTa(O) in darkness and under 400 nm light. (e) TA kinetics with femtosecond resolution for COF-PyTa, COF-PyTa(Sc), and COF-PyTa(6 M) at excitation peaks (690, 698, and 680 nm), showing average relaxation lifetimes. (f) EIS Nyquist plots in darkness.

conducted on the COF-PyTa(W) side of the membrane samples. Initially, N 1s XPS spectra indicated that protonated  $-\text{C}=\text{NH}^+-$  constituted approximately 57% of the total nitrogen content, indicating significant surface protonation. This percentage decreased to 49.4% after 600 s of etching and further to 36.5% after 1860 s. Remarkably, protonated  $-\text{C}=\text{NH}^+-$  became undetectable after 2160 s, approximately halfway through the total etching time required to reach the full thickness of the membrane. This pattern illustrates a progressive reduction in protonation from the COF-PyTa(W) side toward the COF-PyTa(O) side, culminating in the absence of protonated  $-\text{C}=\text{NH}^+-$  at the midpoint of the membrane (Figures 1d and S11). To elucidate the formation mechanism of veridical gradient protonated membrane structures, we analyzed membranes synthesized using 1.5 and 6 M acetic acid. N 1s XPS spectra revealed uniform protonation across the entire membrane rather than a gradient structure (Figure S13). We hypothesized that the thinness of the membrane synthesized using 1.5 M acetic acid (150 nm) facilitated full contact with the acid solution. Conversely, the

higher acid concentration (6 M) promoted the more extensive diffusion of acetic acid into the organic phase, resulting in symmetrical protonation. To deepen our understanding of the protonation process, we compared in situ protonation with postprotonation methods. For this comparison, we synthesized membranes catalyzed by scandium triflate ( $\text{Sc}(\text{OTf})_3$ ), referred to as COF-PyTa(Sc) (Figures S14 and S15). ATR-FTIR spectra indicated that the  $-\text{C}=\text{N}-$  bonds in these membranes remained predominantly unprotonated (Figure S16). Further experiments with COF-PyTa(Sc) membranes treated with increasing acetic acid concentrations from 3 M to pure acetic acid showed escalating peak intensities at 1735 and 1665  $\text{cm}^{-1}$  (Figure S17). Powder X-ray diffraction (PXRD) analysis of the ground COF-PyTa membrane revealed sharp, well-defined, higher-order reflections indicative of high crystallinity. These patterns were Pawley refined by using an AA-stacked model in a  $C2/m$  configuration tailored for the protonated COF structure, achieving satisfactory agreement factors. PXRD patterns of COF-PyTa(Sc) and those treated with 9 M acetic acid exhibited a noticeable shift at the 100 peak compared to

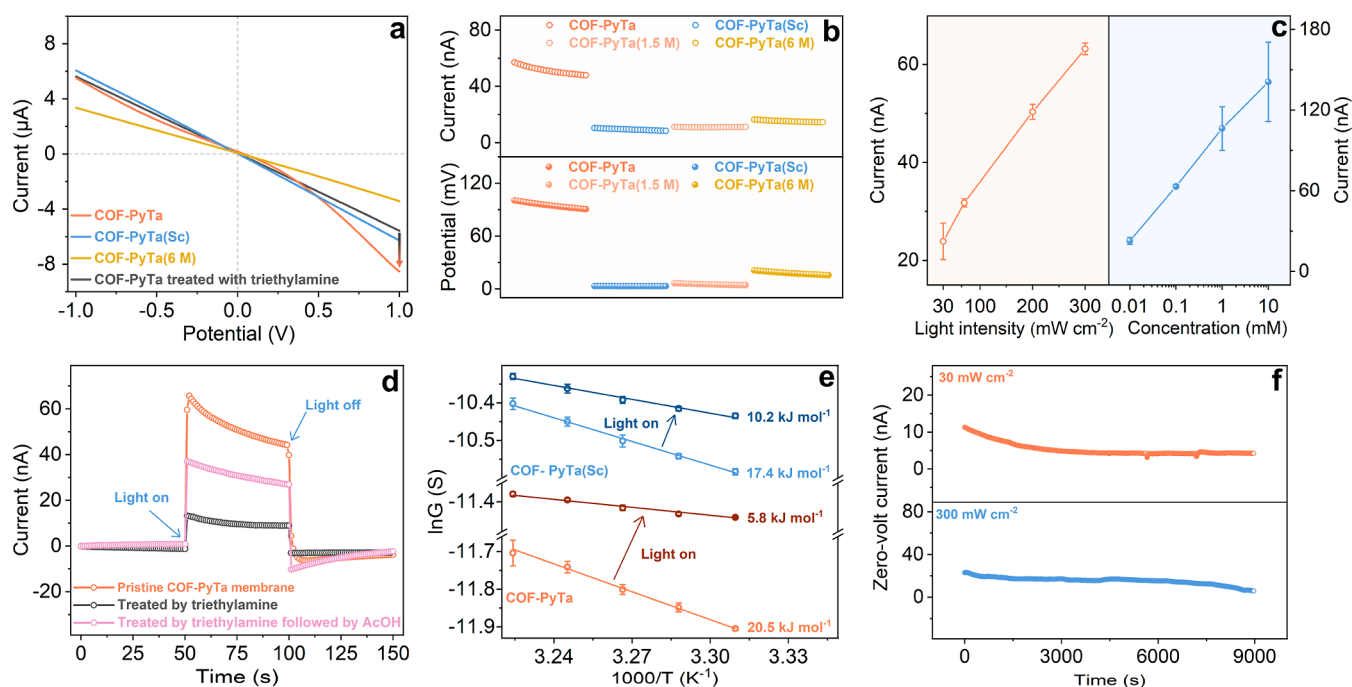


**Figure 3.** Evaluation of light-driven ion transport. (a) I–V curves for a symmetric 1 mM KCl solution. (b) Performance comparison of light-driven ion transport across different membrane types under a Xenon lamp with a power density of 200 mW cm<sup>-2</sup> and a 0.1 mM KCl solution. (c) Dependence of current amplitude on light intensity and KCl concentration: current measurements at different light intensities with a 0.1 mM KCl solution (left) and at various KCl concentrations under constant illumination of 300 mW cm<sup>-2</sup> (right). (d) I–t traces for the COF-PyTa membrane in both dark and illuminated (200 mW cm<sup>-2</sup>) conditions before and after various treatments. (e) Activation energy variations for ion transport through the membrane, measured before and after light exposure. (f) Long-term stability of light-driven ion transport in the COF-PyTa membrane, assessed using a symmetric 0.5 mM KCl solution.

COF-PyTa, closely aligning with the pattern of the non-protonated AA-stacked model in a C2/m configuration (Figures 1f, S18–S20 and Tables S2–S5). Transmission electron microscopy (TEM) imaging revealed interlayer spacings of 0.4 and 0.38 nm for COF-PyTa and COF-PyTa(Sc) membranes, respectively, confirming their lattice differences (Figure 1g,h). These findings suggest that the protonated imine linkages in COF-PyTa resulted from in situ acid-catalyzed condensation, preserving the lattice parameters of the protonated COF structure.

**Membrane Optical Property Investigation.** To evaluate the effects of gradient protonation on the photoadsorptive properties, optical bandgap, energy level alignment, and excited state lifetimes of the COF membrane, we performed extensive characterizations. The UV–vis absorption spectrum of COF-PyTa(W) exhibited enhanced broadening and a significant redshift compared to those of COF-PyTa(O) and COF-PyTa(Sc). Bandgap energies, derived from Tauc plots, indicated that protonation reduces the bandgap: 2.12 eV for COF-PyTa(W), 2.16 eV for COF-PyTa(O), and 2.21 eV for COF-PyTa(Sc) (Figure S21). Density functional theory (DFT) calculations for both the nonprotonated COF-PyTa and its protonated forms—1/4, 1/2, and fully—demonstrated decreases in both the conduction band minimum (CBM) and valence band maximum (VBM), leading to bandgap reductions from 1.14 to 0.97, 0.77, and 0.40 eV, respectively. These reductions were driven by the distinct donor–acceptor contrast between the imine-linked building blocks and their protonated counterparts (Figures 2a and S22). This facilitated the formation of continuous interlayer type-II heterojunctions along the protonation gradient, enhancing interlayer hybridization.<sup>62,65</sup> Ultraviolet photoelectron spectroscopy (UPS)

supported these theoretical predictions by displaying varied energy levels across different sides of the membrane (Figures 2b and S23). The defined bandgap energies and specific localizations of the CBM on the protonated side and the VBM on the nonprotonated side confirmed the formation of type-II heterojunctions (Figure 2c). Kelvin probe force microscopy (KPFM) measurements conducted under dark conditions revealed a potential difference of about 40 mV between the COF-PyTa(O) and COF-PyTa(W) sides (Figures 2d, S24, and S25). This difference suggests the presence of an inherent electric field within the membrane. The lower surface potential observed on the COF-PyTa(O) side aligns consistently with the band alignment depicted in Figure 3c. Upon illumination with superband-gap light, both sides exhibited a significant negative surface photovoltage signal (Figure S25), which directly supports the occurrence of photoinduced charge separation within the COF-PyTa membrane. When the COF-PyTa(O) side was illuminated, a potential drop of approximately 65 mV was observed (Figures 2d and S24). This further increased the potential difference between the two sides, confirming the presence of a photoinduced driving force that potentially facilitates ion transport. In comparison, illuminating the COF-PyTa(6 M) resulted in a potential decrease of about 45 mV, which is less than that observed in the COF-PyTa membrane (Figure S26). This comparison underscores the advantages of gradient protonation in enhancing light-driven ion transport. Transient absorption spectroscopy revealed prolonged exciton relaxation times for COF-PyTa (190 ps) in comparison to those of COF-PyTa(Sc) (70 ps) and COF-PyTa(6 M) (131 ps), which is consistent with the SPV measurements (Figure 2e). Electrochemical impedance spectroscopy (EIS) Nyquist plots indicated smaller

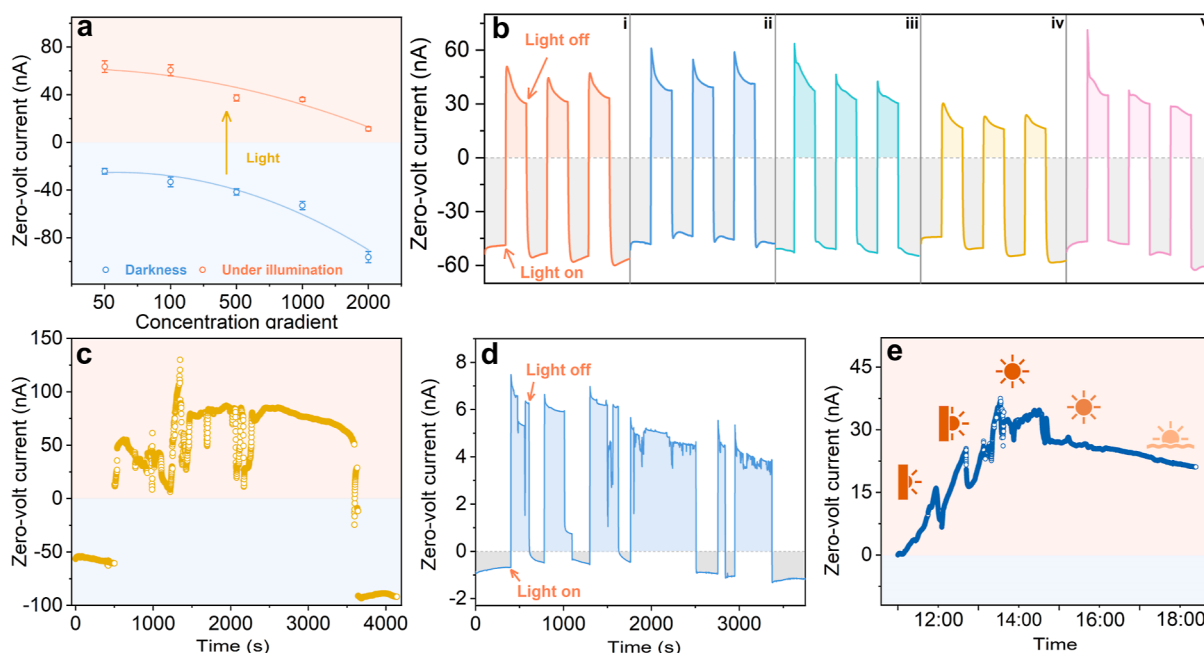


**Figure 4.** Ion pump performance evaluation. (a) Zero-volt current as a function of KCl concentration gradient, from 50-fold to 2000-fold, illustrating the COF-PyTa-based ion pump's capacity to transport ions against a gradient as steep as 2000-fold. (b) Cyclic zero-volt currents recorded under alternating illumination through a COF-PyTa membrane against a 1000-fold salt concentration gradient for (i) KCl, (ii) NaCl, (iii) MgCl<sub>2</sub>, (iv) CaCl<sub>2</sub>, and (v) a quaternary mixture (equal molarity of each), highlighting concentration differences between 1 mM and 1  $\mu$ M, under a 400 mW cm<sup>-2</sup> Xenon lamp. The gray background indicates passive diffusion currents, while the colored background delineates active ion pump currents. (c) Zero-volt current trace across the COF-PyTa membrane when exposed to sunlight, with a 1000-fold KCl concentration gradient (1 mM and 1  $\mu$ M). (d) Cyclic zero-volt currents measured with alternating exposure to natural sunlight through a COF-PyTa membrane from a low concentration of 0.1  $\mu$ M (0.025  $\mu$ M each of KCl, NaCl, CaCl<sub>2</sub>, and MgCl<sub>2</sub>) to 2  $\mu$ M in a quaternary mixture (0.5  $\mu$ M each). The gray background indicates passive diffusion currents, while the colored background delineates active ion pump currents. To verify the membrane's excellent photoreactive reversibility, we specifically varied the time intervals to assess the ion pump performance of the membrane. (e) Zero-volt current trace across the COF-PyTa membrane under sunlight illumination using symmetric water samples treated by primary reverse osmosis with a conductivity of 1.2  $\mu$ S cm<sup>-1</sup>.

arc radii in COF-PyTa compared to those in COF-PyTa(Sc) and COF-PyTa(6 M), with resistances of 112.5, 208.2, and 121.7  $\Omega$ , respectively (Figure 2f), highlighting enhanced light absorption and electron transfer efficiency in the COF membrane with vertical gradient protonation.

**Light-Driven Ion Transmembrane Transport.** To investigate ion transport through vertically aligned COF membranes, samples were examined in a two-compartment electrochemical cell filled with 5 mL of a 1 mM KCl solution in each compartment. The choice of KCl was intentional to minimize spontaneous electric fields at the membrane interfaces due to the similar diffusion coefficients of K<sup>+</sup> and Cl<sup>-</sup> ions.<sup>64–67</sup> Ionic currents were monitored by using Ag/AgCl electrodes. Under scanning voltage, the COF-PyTa membrane displayed a rectified current–voltage (I–V) response, with an ionic current rectification ratio of about 1.5 at  $\pm 1.0$  V at a symmetric 1 mM KCl solution, suggesting an asymmetric protonation within the membrane (Figure S27). This was supported by the observation that rectification effects disappeared after a brief treatment with a triethylamine solution. Moreover, membranes synthesized with 6 M acetic acid showed nearly symmetrical protonation, and the non-protonated COF-PyTa(Sc) exhibited nonrectified I–V responses (Figures 3a and S27).

Ion transport experiments induced by light were performed to assess the photoresponse of the COF membranes under unilateral illumination from a Xenon lamp (Figure S28) while maintaining consistent ionic concentrations across the

membranes (Figures S29 and S30). The membranes produced significant currents and voltages without the need for an external bias (Figure 3b) and demonstrated substantial switching capabilities, toggling on and off in response to the light with varied signal amplitudes in current–time (I–t) and voltage–time (V–t) traces (Figure S31). Current amplitude increased linearly with both light intensity and KCl concentration (Figures 3c, S32 and S33). Specifically, when illuminated from the COF-PyTa(O) side, the COF-PyTa membrane showed reversible increases in current and voltage, approximately  $51 \pm 3$  nA and  $95 \pm 3$  mV, respectively. These increases were significantly higher—3 to 5 times for current and 5 to 30 times for voltage—compared to those observed with other COF membranes synthesized with different catalysts. Treatment of the COF-PyTa(W) side with triethylamine led to a reduction in the photoinduced current to 9 nA. However, immersion in acetic acid on the same side increased the light-induced current to 27 nA (Figure 3d). These observations highlight the critical role of asymmetric protonation in enhancing light-responsive ionic transport. This conclusion is supported by ATR-FTIR analyses, which demonstrate the reversible protonation and deprotonation of the imine linkages (Figure S34). Additionally, changes in solution pH—whether increased or decreased—negatively affect the membrane's ability to facilitate light-driven ion transport, as variations in pH disrupt the necessary protonation gradient (Figures S35 and S36). To demonstrate the broader utility of protonation gradients in enhancing the light

responsiveness of membranes, we postprotonated the initially nonprotonated COF-PyTa(Sc) membrane using a 9 M acetic acid solution. ATR-FTIR spectroscopy confirmed that the membrane achieved full protonation after a 10 min treatment. Light-responsive ion transport tests revealed that the photocurrent followed a volcano-shaped curve relative to the duration of acid treatment, initially increasing and then decreasing, with peak photocurrent observed at 5 min. This peak performance was comparable to that of COF-PyTa, suggesting that membranes with a half-protonated thickness provide the best light-responsive ion transport, assuming constant diffusivity of acid molecules within the membrane (Figures S37 and S38). To further validate this, we synthesized a series of COF membranes with varying thicknesses by adjusting the monomer concentrations as membrane thickness influences the protonation gradient. The COF membrane with an approximate thickness of 360 nm, where half of the membrane was protonated, demonstrated optimal light-responsive ion transport (Figures S5 and S39).

Further investigations into the effects of asymmetric protonation on the activation energy for light-induced ion transport revealed a more significant reduction in the activation energy ( $\Delta E_a$ ) for COF-PyTa compared to that for COF-PyTa(Sc), with reductions of 14.7 and 7.2 kJ mol<sup>-1</sup>, respectively (Figure 3e). In the absence of illumination, the COF-PyTa membrane exhibits a higher ion transmembrane activation barrier than the COF-PyTa(Sc) variant. This elevated barrier is primarily attributed to the partial protonation of imine linkages, which leads to the Donnan exclusion effect, impeding K<sup>+</sup> transport along the ion transfer path. However, the protonation gradient plays a critical role in enhancing the membrane's photoresponsive properties. Upon illumination, the membrane with a protonation gradient generates a stronger built-in electric field, which facilitates ion transport and subsequently lowers the activation energy barrier under illuminated conditions.

In addition to its excellent light responsiveness, the membrane demonstrated long-term stability in light-driven ion transport, effectively concentrating ions on one side while depleting them from the other (Figure 3f). SEM images confirmed that the morphology of the COF-PyTa membrane remained stable over time. Moreover, ATR-FTIR and XPS spectra revealed that the relative intensity of the  $-C=NH^+$  peak compared to the  $-C=N-$  peak remained consistent before and after prolonged irradiation, indicating the membrane's chemical stability (Figure S40). We also assessed the membrane's antifouling properties against *Escherichia coli* (*E. coli*), a common fouling agent in water systems. After 1 week of exposure to natural light, no significant bacterial colonization was observed under SEM (Figure S41). This suggests that the membrane possesses strong antifouling properties, likely due to its photoreactive nature, which may generate reactive oxygen species upon light exposure, inhibiting bacterial growth.

**Ion Pump Performance Evaluation.** To evaluate the COF-PyTa membrane's ion pumping performance, we conducted experiments with a 1  $\mu$ M KCl solution on the COF-PyTa(O) side and solutions with concentrations up to 2 mM on the COF-PyTa(W) side (Figure S42). Without light, the membrane showed a negative current due to passive ion diffusion. Under illumination, ion transport was activated on the lower concentration side, reversing the direction of passive diffusion and improving pumping capability with increased

light intensity (Figures 4a and S43–S45). Specifically, at 500 mW cm<sup>-2</sup> light intensity, the membrane reversed the current from approximately  $-0.1$  to  $0.01$   $\mu$ A, overcoming a 2000-fold concentration gradient with a pumping rate of about  $3.2 \times 10^{12}$  ions s<sup>-1</sup> cm<sup>-2</sup>, making it one of the most efficient artificial ion pumps available (Figure S46 and Table S1). In contrast, the nonprotonated COF-PyTa(Sc) membrane could only pump ions against a 50-fold KCl concentration gradient under identical conditions, highlighting the importance of asymmetric protonation in enhancing ion pumping efficiency (Figure S47). Additionally, the COF-PyTa-based pump exhibited quick and stable light-responsive behavior across various ions, including NaCl, CaCl<sub>2</sub>, and MgCl<sub>2</sub>, even under a 1000-fold concentration gradient, suggesting its utility in desalination applications (Figures 4b and S48). To this end, we further evaluated its pumping capability using a mixed salt solution. Under a 400 mW cm<sup>-2</sup> xenon lamp, the membrane effectively pumped ions from an initial concentration of 1  $\mu$ M (0.25  $\mu$ M each of KCl, NaCl, CaCl<sub>2</sub>, and MgCl<sub>2</sub>) to 1 mM (0.25 mM each), as evidenced by the reversal of the current direction (Figure 4b). To further evaluate its practical performance, we tested the ion pumping efficiency of the COF-PyTa membrane under natural sunlight, with light intensities ranging from 3.0 to 82.3 W m<sup>-2</sup> (Figure S49). The membrane can continuously pump a KCl solution from 1  $\mu$ M (39 ppb for K<sup>+</sup>) to 1 mM (39 ppm for K<sup>+</sup>), demonstrating its ability to reduce ion concentration from at least 19.5 ppm to 39 ppb, thus showcasing its desalination potential (Figure 4c). These variations in intensity were attributed to cloud cover and the movement of the sun. We then tested its performance in deep desalination scenarios using a mixed salt solution from a low concentration side of 0.1  $\mu$ M (0.025  $\mu$ M each of KCl, NaCl, CaCl<sub>2</sub>, and MgCl<sub>2</sub>) to 2  $\mu$ M (0.5  $\mu$ M each). Under natural sunlight, the membrane successfully reversed the current direction, indicating its capability to lower ion concentrations at the parts per billion level (Figures 4d and S50). Furthermore, the COF-PyTa membrane proved effective in concentrating ions from water that had been initially treated by primary reverse osmosis with a conductivity of 1.2  $\mu$ S cm<sup>-1</sup>, highlighting its high desalination efficiency (Figure 4e). This performance was further validated by reducing ion concentrations by approximately 91% to 6.9 ppb from an initial concentration of 79.4 ppb KCl after 3 h of sunlight exposure. To demonstrate the practical applicability of our desalination device, we carried out a continuous operational experiment. The results showcased effective ion transport even under daytime cloudy conditions, with a light intensity of 5 to 10 mW cm<sup>-2</sup>. At night, the process was efficiently sustained by using laboratory lighting with a light intensity of 2.5 mW cm<sup>-2</sup> (Figure S51). To rule out the influence of a temperature gradient—which might develop between the solutions in the two reservoirs due to asymmetric illumination during desalination—our experiments were carefully structured. Results indicate that after 1 h of irradiation at a light intensity of 500 mW cm<sup>-2</sup>, the solution temperature was only about 0.5 °C higher compared to conditions without irradiation (Figure S52). According to the principle of entropy increase, ions tend to migrate from areas of lower to higher temperatures. This would contradict the observed ion transport in our ion pump, where ions move from the side with lower concentration to the side with higher concentration. Consequently, we can conclude that the slight temperature increase does not contribute to the desalination process.

## CONCLUSIONS

We have successfully developed COF membranes with both intralayer and interlayer heterojunction structures through the vertical gradient protonation of imine linkages. These membranes exhibit improved light absorption and sustain a long-lived charge-separated state characterized by rapid light responsiveness and pumping efficiency. A significant light-induced electric field within the membranes drives ion transport across a 2000-fold concentration gradient, markedly enhancing the deep desalination efficiency. Under natural sunlight, these membranes can further concentrate ions from water that had been initially treated by primary reverse osmosis. Our versatile synthesis method for asymmetrically protonated COF membranes can be extended to various monomers such as 2,5-thiophenedicarboxaldehyde and thieno-[3,2-b]thiophene-2,5-dicarboxaldehyde (Figures S53–S62), demonstrating superior light-responsive ion transport capabilities. Future research focusing on optimizing these building units is anticipated to further improve ion pump efficiency, offering a cost-effective, robust, and environmentally friendly solution for advanced desalination technologies.

## ASSOCIATED CONTENT

### Supporting Information

The Supporting Information is available free of charge at <https://pubs.acs.org/doi/10.1021/jacs.4c12829>.

Experimental procedures, materials, characterization, ion-pumping measurement, light-responsive transmembrane ion transport evaluation, ion rectification measurement, DFT calculations, membrane digital photographs, membrane wettability assessment, SEM image, HR-TEM image, ATR-FTIR spectra, XPS spectra, N<sub>2</sub> sorption isotherms, XRD patterns, UV–vis spectra and corresponding Tauc plots, UPS spectra, KPFM images, SPV spectra, Xenon lamp spectrum, and table comparing ion pumping systems (PDF)

## AUTHOR INFORMATION

### Corresponding Authors

**Sai Wang** – Hangzhou Institute of Advanced Studies, Zhejiang Normal University, Hangzhou 310015, China;  
Email: [wangsai@zju.edu.cn](mailto:wangsai@zju.edu.cn)

**Qi Sun** – Zhejiang Provincial Key Laboratory of Advanced Chemical Engineering Manufacture Technology, College of Chemical and Biological Engineering, Zhejiang University, Hangzhou 310058, China; [orcid.org/0000-0002-1698-8741](https://orcid.org/0000-0002-1698-8741); Email: [sunqichs@zju.edu.cn](mailto:sunqichs@zju.edu.cn)

### Authors

**Weipeng Xian** – Zhejiang Provincial Key Laboratory of Advanced Chemical Engineering Manufacture Technology, College of Chemical and Biological Engineering, Zhejiang University, Hangzhou 310058, China

**Xiaoyi Xu** – State Key Laboratory of Silicon and Advanced Semiconductor Materials, Department of Polymer Science and Engineering, Zhejiang University, Hangzhou 310058, China;  
[orcid.org/0000-0002-7372-9287](https://orcid.org/0000-0002-7372-9287)

**Yongxin Ge** – State Key Laboratory of Catalysis, Dalian Institute of Chemical Physics, Chinese Academy of Sciences, Dalian 116023, China; University of Chinese Academy of Sciences, Beijing 100049, China

**Zhiwei Xing** – Zhejiang Provincial Key Laboratory of Advanced Chemical Engineering Manufacture Technology, College of Chemical and Biological Engineering, Zhejiang University, Hangzhou 310058, China

**Zhuozhi Lai** – Zhejiang Provincial Key Laboratory of Advanced Chemical Engineering Manufacture Technology, College of Chemical and Biological Engineering, Zhejiang University, Hangzhou 310058, China

**Qing-Wei Meng** – Zhejiang Provincial Key Laboratory of Advanced Chemical Engineering Manufacture Technology, College of Chemical and Biological Engineering, Zhejiang University, Hangzhou 310058, China

**Zhifeng Dai** – Key Laboratory of Surface & Interface Science of Polymer Materials of Zhejiang Province, School of Chemistry and Chemical Engineering, Zhejiang Sci-Tech University, Hangzhou 310018, China; Longgang Institute of Zhejiang Sci-Tech University, Wenzhou 325802, China;  
[orcid.org/0000-0002-0733-8317](https://orcid.org/0000-0002-0733-8317)

**Ruotian Chen** – State Key Laboratory of Catalysis, Dalian Institute of Chemical Physics, Chinese Academy of Sciences, Dalian 116023, China

**Ning Huang** – State Key Laboratory of Silicon and Advanced Semiconductor Materials, Department of Polymer Science and Engineering, Zhejiang University, Hangzhou 310058, China;  
[orcid.org/0000-0002-7021-8705](https://orcid.org/0000-0002-7021-8705)

**Shengqian Ma** – Department of Chemistry, University of North Texas, Denton, Texas 76201, United States;  
[orcid.org/0000-0002-1897-7069](https://orcid.org/0000-0002-1897-7069)

Complete contact information is available at:  
<https://pubs.acs.org/doi/10.1021/jacs.4c12829>

## Notes

The authors declare no competing financial interest.

## ACKNOWLEDGMENTS

This work was supported by the National Key Research and Development Program of China (2022YFA1503004), National Science Foundation of China (22421004), and the National Science Foundation of Zhejiang province (LR23B060001 and LY23B060022). We appreciate the assistance of Fang Chen from Analytical Testing Center of the Department of Chemistry, Zhejiang University, in conducting SEM measurements.

## REFERENCES

- (1) Alvarez, P. J. J.; Chan, C. K.; Elimelech, M.; Halas, N. J.; Villagran, D. Emerging Opportunities for Nanotechnology to Enhance Water Security. *Nat. Nanotechnol.* **2018**, *13*, 634–641.
- (2) Ding, L.; Li, L.; Liu, Y.; Wu, Y.; Lu, Z.; Deng, J.; Wei, Y.; Caro, J.; Wang, H. Effective Ion Sieving with Ti<sub>3</sub>C<sub>2</sub>T<sub>x</sub> MXene Membranes for Production of Drinking Water from Seawater. *Nat. Sustain.* **2020**, *3*, 296–302.
- (3) Ou, R.; Zhang, H.; Truong, V. X.; Zhang, L.; Hegab, H. M.; Han, L.; Hou, J.; Zhang, X.; Deletic, A.; Jiang, L.; Simon, G. P.; Wang, H. A Sunlight-Responsive Metal–Organic Framework System for Sustainable Water Desalination. *Nat. Sustain.* **2020**, *3*, 1052–1058.
- (4) Shannon, M. A.; Bohn, P. W.; Elimelech, M.; Georgiadis, J. G.; Marinas, B. J.; Mayes, A. M. Science and Technology for Water Purification in the Coming Decades. *Nature* **2008**, *452*, 301–310.
- (5) Heiranian, M.; Fan, H.; Wang, L.; Lu, X.; Elimelech, M. Mechanisms and Models for Water Transport in Reverse Osmosis Membranes: History, Critical Assessment, and Recent Developments. *Chem. Soc. Rev.* **2023**, *52*, 8455–8480.



- (6) Wen, Y.; Dai, R.; Li, X.; Zhang, X.; Cao, X.; Wu, Z.; Lin, S.; Tang, C. Y.; Wang, Z. Metal-Organic Framework Enables Ultra-selective Polyamide Membrane for Desalination and Water Reuse. *Sci. Adv.* **2022**, *8*, No. eabm4149.
- (7) Smith, R. C.; Sengupta, A. K. Integrating Tunable Anion Exchange with Reverse Osmosis for Enhanced Recovery During Inland Brackish Water Desalination. *Environ. Sci. Technol.* **2015**, *49*, 5637–5644.
- (8) Alkhadra, M. A.; Su, X.; Suss, M. E.; Tian, H.; Guyes, E. N.; Shocron, A. N.; Conforti, K. M.; De Souza, J. P.; Kim, N.; Tedesco, M.; Khoiruddin, K.; Wenten, I. G.; Santiago, J. G.; Hatton, T. A.; Bazant, M. Z. Electrochemical Methods for Water Purification, Ion Separations; and Energy Conversion. *Chem. Rev.* **2022**, *122*, 13547–13635.
- (9) Zuo, K.; Garcia-Segura, S.; CerrÓN-Calle, G. A.; Chen, F.-Y.; Tian, X.; Wang, X.; Huang, X.; Wang, H.; Alvarez, P. J. J.; Lou, J.; Elimelech, M.; Li, Q. Electrified Water Treatment: Fundamentals and Roles of Electrode Materials. *Nat. Rev. Mater.* **2023**, *8*, 472–490.
- (10) Inoue, K.; Ono, H.; Abe-Yoshizumi, R.; Yoshizawa, S.; Ito, H.; Kogure, K.; Kandori, H. A Light-Driven Sodium Ion Pump in Marine Bacteria. *Nat. Commun.* **2013**, *4*, 1678.
- (11) Mous, S.; Gotthard, G.; Ehrenberg, D.; Sen, S.; Weinert, T.; Johnson, P. J. M.; James, D.; Nass, K.; Furrer, A.; Kekilli, D.; Ma, P.; BrÜNle, S.; Casadei, C. M.; Martiel, I.; Dworkowski, F.; Gashi, D.; Skopintsev, P.; Wraniak, M.; Knopp, G.; Panepucci, E.; Panneels, V.; Cirelli, C.; Ozerov, D.; Schertler, G. F. X.; Wang, M.; Milne, C.; Standfuss, J.; Schapiro, L.; Heberle, J.; Nogly, P. Dynamics and Mechanism of a Light-Driven Chloride Pump. *Sci. Adv.* **2022**, *375*, 845–851.
- (12) Jiang, Y.; Ma, W.; Qiao, Y.; Xue, Y.; Lu, J.; Gao, J.; Liu, N.; Wu, F.; Yu, P.; Jiang, L.; Mao, L. Metal-Organic Framework Membrane Nanopores as Biomimetic Photoresponsive Ion Channels and Photodriven Ion Pumps. *Angew. Chem., Int. Ed.* **2020**, *59*, 12795–12799.
- (13) Li, C.; Zhai, Y.; Jiang, H.; Li, S.; Liu, P.; Gao, L.; Jiang, L. Bioinspired Light-Driven Chloride Pump with Helical Porphyrin Channels. *Nat. Commun.* **2024**, *15*, 832.
- (14) Liu, S.-H.; Hu, C.-K.; Lu, J.-L.; Lu, X.; Lu, C.-X.; Yao, J.; Chen, X.-C.; Jiang, L. Superstructured Optoionic Heterojunctions for Promoting Ion Pumping Inspired by Photoreceptor Cells. *ACS Nano* **2024**, *18*, 9053–9062.
- (15) Nie, X.; Hu, Z.; Xiao, T.; Li, L.; Jin, J.; Liu, K.; Liu, Z. Light-Powered Ion Pumping in a Cation-Selective Conducting Polymer Membrane. *Angew. Chem., Int. Ed.* **2022**, *61*, No. e202201138.
- (16) Niu, M.; Chen, Y.; Chen, F.; Zhao, C.; Yang, Y.; Xu, Y.; Feng, J. Light-Driven Ion Transport Through Single-Heterojunction Nanopores. *Nano Lett.* **2023**, *23*, 1010–1016.
- (17) Shao, B.; Fu, H.; Aprahamian, I. A. Molecular Anion Pump. *Science* **2024**, *385*, 544–549.
- (18) Xiao, K.; Chen, L.; Chen, R.; Heil, T.; Lemus, S. D. C.; Fan, F.; Wen, L.; Jiang, L.; Antonietti, M. Artificial Light-Driven Ion Pump for Photoelectric Energy Conversion. *Nat. Commun.* **2019**, *10*, 74.
- (19) Yang, J.; Hu, X.; Kong, X.; Jia, P.; Ji, D.; Quan, D.; Wang, L.; Wen, Q.; Lu, D.; Wu, J.; Jiang, L.; Guo, W. Photo-Induced Ultrafast Active Ion Transport Through Graphene Oxide Membranes. *Nat. Commun.* **2019**, *10*, 1171.
- (20) Yang, J.; Liu, P.; He, X.; Hou, J.; Feng, Y.; Huang, Z.; Yu, L.; Li, L.; Tang, Z. Photodriven Active Ion Transport Through a Janus Microporous Membrane. *Angew. Chem., Int. Ed.* **2020**, *59*, 6244–6248.
- (21) Xiao, K.; Jiang, L.; Antonietti, M. Ion Transport in Nanofluidic Devices for Energy Harvesting. *Joule* **2019**, *3*, 2364–2380.
- (22) Wang, J.; Song, Z.; He, M.; Qian, Y.; Wang, D.; Cui, Z.; Feng, Y.; Li, S.; Huang, B.; Kong, X.-Y.; Han, J.; Wang, L. Light-Responsive and Ultrapermeable Two-Dimensional Metal-Organic Framework Membrane for Efficient Ionic Energy Harvesting. *Nat. Commun.* **2024**, *15*, 2125.
- (23) Jin, X.; Zeng, Y.; Zhou, M.; Quan, D.; Jia, M.; Liu, B.; Cai, K.; Kang, L.; Kong, X.; Wen, L.; Jiang, L. Photo-Driven Ion Directional Transport across Artificial Ion Channels: Band Engineering of WS<sub>2</sub> via Peptide Modification. *Small* **2024**, *20*, 2401264.
- (24) Corra, S.; Bakić, M. T.; Groppi, J.; Baroncini, M.; Silvi, S.; Penocchio, E.; Esposito, M.; Credi, A. Kinetic and Energetic Insights into the Dissipative Non-Equilibrium Operation of an Autonomous Light-Powered Supramolecular Pump. *Nat. Nanotechnol.* **2022**, *17*, 746–751.
- (25) Liu, P.; Zhou, T.; Teng, Y.; Fu, L.; Hu, Y.; Lin, X.; Kong, X.-Y.; Jiang, L.; Wen, L. Light-Induced Heat Driving Active Ion Transport Based on 2D MXene Nanofluids for Enhancing Osmotic Energy Conversion. *CCS Chem.* **2021**, *3*, 1325–1335.
- (26) Asif, M. B.; Kim, S.; Nguyen, T. S.; Mahmood, J.; Yavuz, C. T. Covalent Organic Framework Membranes and Water Treatment. *J. Am. Chem. Soc.* **2024**, *146*, 3567–3584.
- (27) Burke, D. W.; Jiang, Z.; Livingston, A. G.; Dichtel, W. R. 2D Covalent Organic Framework Membranes for Liquid-Phase Molecular Separations: State of the Field, Common Pitfalls, and Future Opportunities. *Adv. Mater.* **2024**, *36*, No. e2300525.
- (28) Cao, L.; Chen, I. C.; Chen, C.; Shinde, D. B.; Liu, X.; Li, Z.; Zhou, Z.; Zhang, Y.; Han, Y.; Lai, Z. Giant Osmotic Energy Conversion through Vertical-Aligned Ion-Permeable Nanochannels in Covalent Organic Framework Membranes. *J. Am. Chem. Soc.* **2022**, *144*, 12400–12409.
- (29) Knebel, A.; Caro, J. Metal-Organic Frameworks and Covalent Organic Frameworks as Disruptive Membrane Materials for Energy-Efficient Gas Separation. *Nat. Nanotechnol.* **2022**, *17*, 911–923.
- (30) Liu, T.; Zhang, Y.; Shan, Z.; Wu, M.; Li, B.; Sun, H.; Su, G.; Wang, R.; Zhang, G. Covalent Organic Framework Membrane for Efficient Removal of Emerging Trace Organic Contaminants from Water. *Nat. Water* **2023**, *1*, 1059–1067.
- (31) Liu, X.; Wang, Z.; Zhang, Q.; Lei, D.; Li, X.; Zhang, Z.; Feng, X. Highly Anion-Conductive Viologen-Based Two-Dimensional Polymer Membranes as Nanopower Generators. *Angew. Chem., Int. Ed.* **2024**, *63*, No. e202409349.
- (32) Sheng, F.; Wu, B.; Li, X.; Xu, T.; Shehzad, M. A.; Wang, X.; Ge, L.; Wang, H.; Xu, T. Efficient Ion Sieving in Covalent Organic Framework Membranes with Sub-2-Nanometer Channels. *Adv. Mater.* **2021**, *33*, 2104404.
- (33) Wang, M.; Zhang, P.; Liang, X.; Zhao, J.; Liu, Y.; Cao, Y.; Wang, H.; Chen, Y.; Zhang, Z.; Pan, F.; Zhang, Z.; Jiang, Z. Ultrafast Seawater Desalination with Covalent Organic Framework Membranes. *Nat. Sustain.* **2022**, *5*, 518–526.
- (34) Xian, W.; Wu, D.; Lai, Z.; Wang, S.; Sun, Q. Advancing Ion Separation: Covalent-Organic-Framework Membranes for Sustainable Energy and Water Applications. *Acc. Chem. Res.* **2024**, *57*, 1973–1984.
- (35) Yin, C.; Liu, M.; Zhang, Z.; Wei, M.; Shi, X.; Zhang, Y.; Wang, J.; Wang, Y. Perpendicular Alignment of Covalent Organic Framework (COF) Pore Channels by Solvent Vapor Annealing. *J. Am. Chem. Soc.* **2023**, *145*, 11431–11439.
- (36) Ying, Y.; Peh, S. B.; Yang, H.; Yang, Z.; Zhao, D. Ultrathin Covalent Organic Framework Membranes via a Multi-Interfacial Engineering Strategy for Gas Separation. *Adv. Mater.* **2022**, *34*, 2104946.
- (37) Zhang, Y.; Wang, H.; Wang, W.; Zhou, Z.; Huang, J.; Yang, F.; Bai, Y.; Sun, P.; Ma, J.; Peng, L. E.; Tang, C. Y.; Shao, L. Engineering Covalent Organic Framework Membranes for Efficient Ionic/Molecular Separations. *Matter* **2024**, *7*, 1406–1439.
- (38) Cheng, Y.-Z.; Ji, W.; Hao, P.-Y.; Qi, X.-H.; Wu, X.; Dou, X.-M.; Bian, X.-Y.; Jiang, D.; Li, F.-T.; Liu, X.-F.; Yang, D.-H.; Ding, X.; Han, B.-H. A Fully Conjugated Covalent Organic Framework with Oxidative and Reductive Sites for Photocatalytic Carbon Dioxide Reduction with Water. *Angew. Chem., Int. Ed.* **2023**, *62*, No. e202308523.
- (39) Krishnaraj, C.; Sekhar Jena, H.; Bourda, L.; Laemont, A.; Pachfule, P.; Roeser, J.; Chandran, C. V.; Borgmans, S.; Rogge, S. M. J.; Leus, K.; Stevens, C. V.; Martens, J. A.; Van Speybroeck, V.; Breynaert, E.; Thomas, A.; Van Der Voort, P. Strongly Reducing (Diarylamino)Benzene-Based Covalent Organic Framework for

Metal-Free Visible Light Photocatalytic H<sub>2</sub>O<sub>2</sub> Generation. *J. Am. Chem. Soc.* **2020**, *142*, 20107–20116.

(40) Li, T.; Zhang, P.-L.; Dong, L.-Z.; Lan, Y.-Q. Post-synthetic Rhodium (III) Complexes in Covalent Organic Frameworks for Photothermal Heterogeneous C–H Activation. *Angew. Chem., Int. Ed.* **2024**, *63*, No. e202318180.

(41) Liu, R.; Chen, Y.; Yu, H.; Položij, M.; Guo, Y.; Sum, T. C.; Heine, T.; Jiang, D. Linkage-Engineered Donor-Acceptor Covalent Organic Frameworks for Optimal Photosynthesis of Hydrogen Peroxide from Water and Air. *Nat. Catal.* **2024**, *7*, 195–206.

(42) Rodriguez-Camargo, A.; Endo, K.; Lotsch, B. V. Celebrating Ten Years of Covalent Organic Frameworks for Solar Energy Conversion: Past, Present And Future. *Angew. Chem., Int. Ed.* **2024**, *63*, No. e202413096.

(43) Wang, Y.-R.; Ding, H.-M.; Sun, S.-N.; Shi, J.-W.; Yang, Y.-L.; Li, Q.; Chen, Y.; Li, S.-L.; Lan, Y.-Q. Light Heat and Electricity Integrated Energy Conversion System: Photothermal-Assisted Co-Electrolysis of CO<sub>2</sub> and Methanol. *Angew. Chem., Int. Ed.* **2022**, *61*, No. e202212162.

(44) Xu, T.; Wang, Z.; Zhang, W.; An, S.; Wei, L.; Guo, S.; Huang, Y.; Jiang, S.; Zhu, M.; Zhang, Y.-B.; Zhu, W.-H. Constructing Photocatalytic Covalent Organic Frameworks with Aliphatic Linkers. *J. Am. Chem. Soc.* **2024**, *146*, 20107–20115.

(45) Yan, X.; Lyu, S.; Xu, X.-Q.; Chen, W.; Shang, P.; Yang, Z.; Zhang, G.; Chen, W.; Wang, Y.; Chen, L. Superhydrophilic 2D Covalent Organic Frameworks as Broadband Absorbers for Efficient Solar Steam Generation. *Angew. Chem., Int. Ed.* **2022**, *61*, No. e202201900.

(46) Yu, H.; Zhang, F.; Chen, Q.; Zhou, P. K.; Xing, W.; Wang, S.; Zhang, G.; Jiang, Y.; Chen, X. Vinyl-Group-Anchored Covalent Organic Framework for Promoting the Photocatalytic Generation of Hydrogen Peroxide. *Angew. Chem., Int. Ed.* **2024**, *63*, No. e202402297.

(47) Zhang, X.; Cheng, S.; Chen, C.; Wen, X.; Miao, J.; Zhou, B.; Long, M.; Zhang, L. Keto-Anthraquinone Covalent Organic Framework for H<sub>2</sub>O<sub>2</sub> Photosynthesis with Oxygen and Alkaline Water. *Nat. Commun.* **2024**, *15*, 2649.

(48) Zou, L.; Chen, Z.-A.; Si, D.-H.; Yang, S.-L.; Gao, W.-Q.; Wang, K.; Huang, Y.-B.; Cao, R. Boosting CO<sub>2</sub> Photoreduction via Regulating Charge Transfer Ability in a One-Dimensional Covalent Organic Framework. *Angew. Chem., Int. Ed.* **2023**, *62*, No. e202309820.

(49) Luo, R.; Lv, H.; Liao, Q.; Wang, N.; Yang, J.; Li, Y.; Xi, K.; Wu, X.; Ju, H.; Lei, J. Intrareticular Charge Transfer Regulated Electrochemiluminescence of Donor-Acceptor Covalent Organic Frameworks. *Nat. Commun.* **2021**, *12*, 6808.

(50) Qian, Y.; Han, Y.; Zhang, X.; Yang, G.; Zhang, G.; Jiang, H.-L. Computation-Based Regulation of Excitonic Effects in Donor-Acceptor Covalent Organic Frameworks for Enhanced Photocatalysis. *Nat. Commun.* **2023**, *14*, 3083.

(51) Shu, C.; Yang, X.; Liu, L.; Hu, X.; Sun, R.; Yang, X.; Cooper, A. I.; Tan, B.; Wang, X. Mixed-Linker Strategy for the Construction of Sulfone-Containing D-A-A Covalent Organic Frameworks for Efficient Photocatalytic Hydrogen Peroxide Production. *Angew. Chem., Int. Ed.* **2024**, *63*, No. e202403926.

(52) Barré, E.; Dandu, M.; Kundu, S.; Sood, A.; Da Jornada, F. H.; Raja, A. Engineering Interlayer Hybridization in Van Der Waals Bilayers. *Nat. Rev. Mater.* **2024**, *9*, 499–508.

(53) Tang, Y.; Gu, J.; Liu, S.; Watanabe, K.; Taniguchi, T.; Hone, J.; Mak, K. F.; Shan, J. Tuning Layer-Hybridized Moire Excitons by the Quantum-Confined Stark Effect. *Nat. Nanotechnol.* **2021**, *16*, 52–57.

(54) Ascherl, L.; Evans, E. W.; Gorman, J.; Orsborne, S.; Bessinger, D.; Bein, T.; Friend, R. H.; Auras, F. Perylene-Based Covalent Organic Frameworks for Acid Vapor Sensing. *J. Am. Chem. Soc.* **2019**, *141*, 15693–15699.

(55) Dai, L.; Dong, A.; Meng, X.; Liu, H.; Li, Y.; Li, P.; Wang, B. Enhancement of Visible-Light-Driven Hydrogen Evolution Activity of 2D  $\Pi$ -Conjugated Bipyridine-Based Covalent Organic Frameworks

via Post-Protonation. *Angew. Chem., Int. Ed.* **2023**, *62*, No. e202300224.

(56) Shi, T.; Wang, H.; Li, L.; Zhao, Z.; Wang, C.; Zhang, X.; Xie, Y. Enhanced Photostability in Protonated Covalent Organic Frameworks for Singlet Oxygen Generation. *Matter* **2022**, *5*, 1004–1015.

(57) Yang, J.; Acharjya, A.; Ye, M. Y.; Rabeah, J.; Li, S.; Kochovski, Z.; Youk, S.; Roeser, J.; Gruneberg, J.; Penschke, C.; Schwarze, M.; Wang, T.; Lu, Y.; Van De Krol, R.; Oschatz, M.; Schomacker, R.; Saalfrank, P.; Thomas, A. Protonated Imine-Linked Covalent Organic Frameworks for Photocatalytic Hydrogen Evolution. *Angew. Chem., Int. Ed.* **2021**, *60*, 19797–19803.

(58) Borisova, N. E.; Reshetova, M. D.; Ustynyuk, Y. A. Metal-Free Methods in the Synthesis of Macrocyclic Schiff Bases. *Chem. Rev.* **2007**, *107*, 46–79.

(59) Ascherl, L.; Evans, E. W.; Hennemann, M.; Di Nuzzo, D.; Hufnagel, A. G.; Beetz, M.; Friend, R. H.; Clark, T.; Bein, T.; Auras, F. Solvatochromic Covalent Organic Frameworks. *Nat. Commun.* **2018**, *9*, 3802.

(60) Dong, P.; Xu, X.; Wu, T.; Luo, R.; Kong, W.; Xu, Z.; Yuan, S.; Zhou, J.; Lei, J. Stepwise Protonation of Three-Dimensional Covalent Organic Frameworks for Enhancing Hydrogen Peroxide Photosynthesis. *Angew. Chem., Int. Ed.* **2024**, *63*, No. e202405313.

(61) Zhu, Q.; Shi, L.; Li, Z.; Li, G.; Xu, X. Protonation of an Imine-Linked Covalent Organic Framework for Efficient H<sub>2</sub>O<sub>2</sub> Photosynthesis under Visible Light up to 700 nm. *Angew. Chem., Int. Ed.* **2024**, *63*, No. e202408041.

(62) Tao, X.; Zhao, Y.; Wang, S.; Li, C.; Li, R. Recent Advances and Perspectives for Solar-Driven Water Splitting Using Particulate Photocatalysts. *Chem. Soc. Rev.* **2022**, *51*, 3561–3608.

(63) Zhang, L.; Zhang, J.; Yu, H.; Yu, J. Emerging S-Scheme Photocatalyst. *Adv. Mater.* **2022**, *34*, 2107668.

(64) Liu, P.; Kong, X.-Y.; Jiang, L.; Wen, L. Ion Transport in Nanofluidics under External Fields. *Chem. Soc. Rev.* **2024**, *53*, 2972–3001.

(65) Chen, C.; Liu, D.; He, L.; Qin, S.; Wang, J.; Razal, J. M.; Kotov, N. A.; Lei, W. Bio-Inspired Nanocomposite Membranes for Osmotic Energy Harvesting. *Joule* **2020**, *4*, 247–261.

(66) Chen, W.; Zhou, K.; Wu, Z.; Yang, L.; Xie, Y.; Meng, X.; Zhao, Z.; Wen, L. Ion-Concentration-Hopping Heterolayer Gel for Ultrahigh Gradient Energy Conversion. *J. Am. Chem. Soc.* **2024**, *146*, 13191–13200.

(67) Xian, W.; Zuo, X.; Zhu, C.; Guo, Q.; Meng, Q.-W.; Zhu, X.; Wang, S.; Ma, S.; Sun, Q. Anomalous Thermo-Osmotic Conversion Performance of Ionic Covalent-Organic-Framework Membranes in Response to Charge Variations. *Nat. Commun.* **2022**, *13*, 3386.